

Impact damage of laminated composite with energy dissipation: Part I — Nonhomogenous characteristics

G.C. Sih

Institute of Fracture and Solid Mechanics, Lehigh University, Bethlehem, PA 18015, USA

Abstract

Composite laminates could be made to diffuse penetration energy at predetermined rates in addition to locations. Materials with different hardness and toughness can be stacked in the appropriate sequence to create a more widespread damage pattern. The kinetic energy per unit volume of the laminate could then be reduced to prevent complete perforation.

Analyzed in detail is the failure sequence of a tungsten rod (47 mm long and 14 mm in diameter) impacting a three-layered composite laminate at 1100 m/s. The top layer is a 6 mm thick ceramic (Al_2O_3). Sandwiched in between is a 10 mm thick rubber layer backed up by a 4 mm thick 4340 steel plate. At approximately 10 μs , the tungsten rod is already badly shattered, whereas the ceramic is only fragmented in a layer next to the surface. The ceramic reflects the impact waves which cause damage in the tungsten rod. Within the next 1.50 μs , i.e. 21.5 μs , the dissipated energy density in the rubber increased two orders of magnitude from 32.11 to 33.25×10^2 Pa while those in the ceramic and steel are much smaller. The highest temperature in the ceramic reached about 555°C and that in the back-up steel plate is only 275°C. Upon complete fragmentation of the tungsten rod, a through the thickness cavity is predicted in the ceramic while a mushroom head shaped crack is predicted in the rubber. Interfacial cracks are widespread but the steel layer remained intact.

Presentation is divided into two parts. Part I describes the basic scheme of the methodology and the nonhomogeneous character of response within each layer of the composite laminate. That is the constitutive relation for each material element is derived according to the local strain and strain rate rather than preassumed. Thermal/mechanical interactions are synchronized by application of the isoenergy density theory in nonequilibrium thermomechanics. At 0.15 μs , concentration of energy is detected at the impact site and ceramic/rubber interface. The finite element grid pattern had to be remeshed after 50 μs to account for the discontinuities created by damage at the interphases. Modelled in Part II are the evolution of damage in steps until the tungsten rod is completely destroyed. Nonequilibrium data such as load strain rates, temperatures, dissipation energies, etc. are given numerically and displayed graphically.

1. Introduction

Dynamic response of composite laminates covers an overwhelmingly wide range of problems that could vary from the rudimentary tests to the

sophisticated analyses. Many of the past works can be found in [1–3]. Assessment of the nonhomogeneous character of the damage process becomes problematic because the material constitutive relation and failure criterion must be as-

sumed independently in the classical continuum mechanics approach. There is no rational means to account for the disparities. In principle, predictive models should have the capability to scale the base reference material data to situations other than those tested. That is the conversion of low strain rate uniaxial data to high strain rates and low temperature data to high temperature levels. Such a scheme is inherent in the isoenergy density theory [4,5].

Damage patterns for a single 4340 steel plate 20 mm thick impacted by a tungsten rod at a speed of 1100 m/s have been obtained [6]. Using only tensile specimen data at ambient condition, local temperature of 640°C and latent heat (strain rate of energy dissipation density) of 11 MPa were predicted at 0.35 μ s. Perforation of the plate by plugging was predicted in addition to the phase transformation of the material in a narrow band around the plug. Thickness of the plug is about 40% of that for the plate while a 33% reduction of the tungsten rod was estimated. The rod velocity decreased to 760 m/s at 0.30 μ s. Such details have also been made available for the hypervelocity impact of aluminum plate [7]. Local melting and vaporization of the aluminum were predicted where the estimated strain rates reached as high as 10^8 – 10^9 s $^{-1}$. These findings are in general agreement with the experimental findings. Validation of nonequilibrium temperatures with experiments can be found in [5] for uniaxial specimens under static loadings. More recently, dissipation energy densities were measured [8] for characterizing the failure behavior of composite materials. They describe the degree of internal damage in more realistic terms.

Presented is Part I of this study concerning the impact damage of a tungsten rod striking a three-layered ceramic/rubber/steel composite laminate. The stress and strain response for each material element is determined from a knowledge of the rate change of local volume to surface which couples the exchange between surface and volume energy. It also synchronizes the thermal/mechanical disturbances caused by the impact. The IDA (isoenergy density analysis) program [9] is used to formulate the problem for analyzing the nonhomogenous response of the

composite laminate. The sequence of the damage process will be discussed in Part II [10] where the calculations are carried out until the analysis predicts complete destruction of the tungsten rod.

2. Isoenergy energy theory: finite element size

Two distinct features of the isoenergy density theory are [4,5]:

- Element size remains finite and is determined from the condition of isoenergy density state.
- Temperature is obtained directly from the rate change of volume with surface, isostrain and dissipation energy density.

The term isoenergy refers to the situation where the same energy is transmitted across the orthogonal surfaces of a continuum element. Energy density could still vary from element to element. What the isoenergy density theory establishes is the unique correspondence of energy states regardless of their stress and/or strain dimensionality. No other continuum mechanics theories with energy dissipation possess such capability. The classical theory of plasticity leaves out the dilatational portion of the energy density when making correlation between the uniaxial and multiaxial stress-strain states. Separation of dilatation and distortion is borne out from the property of linear elasticity; it is not valid for nonlinear theories.

2.1. Nonlocal effect

In the isoenergy density theory, the traction \vec{T}_i on a tetrahedron referred to the rectangular coordinates (x, y, z) is given by

$$\vec{T}_i = \sigma_{ij} n_j + \rho(\ddot{u}_i - h_i) \left(\frac{\Delta V}{\Delta A} \right)_n, \quad (1)$$

where σ_{ij} are stress components, \ddot{u}_i are the accelerations and h_i the body force components with ρ being the mass density. The displacement components are u_i . Eq. (1) differs from classical continuum mechanics in that the rate changes of volume with surface $(\Delta V/\Delta A)_n$ or \mathcal{V}_n are no longer assumed to vanish in the limit. It provides the additional length scale parameter that ac-

counts for nonlocal effects. The interaction of the inertia term $\rho \ddot{u}_i$ with \mathcal{V}_n becomes crucial at the impact site where surface energy is being converted into volume energy.

2.2. Energy transmission across surface

When two bodies are impacted, energy transfers from one body to the other across the contact surface or interface. There is an exchange of surface and volume energy density. Let the former be denoted by $(\Delta W/\Delta A)_i$ or \mathcal{S}_i and the latter by $\Delta W/\Delta V$ or \mathcal{W} . They are related as

$$\mathcal{S}_i = \mathcal{V}_i \mathcal{W}, \quad i = x, y, z. \quad (2)$$

The quantities \mathcal{S}_i represent the energy prevailing on the three orthogonal surfaces of an element, while \mathcal{V}_i are the corresponding components of the vector for the rate change of volume with surface. For an isoenergy element the three components \mathcal{S}_i ($i = 1, 2, 3$) are required to be the same. The significance of this requirement will be elaborated subsequently.

2.3. Isoenergy elements

The size and orientation of an isoenergy element can be determined by letting

$$\mathcal{S}_1 = \mathcal{S}_2 = \mathcal{S}_3 \rightarrow \mathcal{S}_0, \quad i = 1, 2, 3, \quad (3)$$

that is the same \mathcal{S}_0 would prevail on all of the three orthogonal surfaces. Since \mathcal{W} is a scalar, it follows from Eq. (2) that

$$\mathcal{V}_1 = \mathcal{V}_2 = \mathcal{V}_3 \rightarrow \mathcal{V}_0. \quad (4)$$

The rate change of volume with surface for an isoenergy element is also the same in all directions. These different size elements could be connected to form a continuous body such that upon deformation there will be no gaps between the conceptual interfaces of the adjacent elements. The proof for the existence of the isoenergy surface made of these elements is given in [4].

2.4. Field equations

In order to emphasize the nonlocal character of the isoenergy density theory, Eq. (1) can be

rewritten in terms of the isostress components τ_{ij} as

$$\frac{\eta}{T_i} = \tau_{ji} n_j, \quad \tau_{ij} \neq \tau_{ji}, \quad (5)$$

in which

$$\tau_{ji} = \sigma_{ji} + \rho(\ddot{u}_i - h_i) \mathcal{V}_j, \quad (6)$$

and τ is not symmetric. The equations of equilibrium expressed in terms of τ_{ij} have the same formal appearance as those in the classical theories, i.e.

$$\frac{\partial \tau_{ji}}{\partial \xi_j} + \rho h_i = \rho \ddot{u}_i, \quad (7)$$

where ξ_i ($i = 1, 2, 3$) refer to the current state coordinates of an element as distinguished from the reference coordinates x_i ($i = 1, 2, 3$). The conservation of energy requires that

$$\begin{aligned} \int_A \rho h_i \dot{u}_i dV + \int_{\Sigma} \frac{\eta}{T_i} \dot{u}_i dA \\ = \int_A \rho \ddot{u}_i \dot{u}_i dV + \frac{d}{dt} \int_A \mathcal{W} dV, \end{aligned} \quad (8)$$

in which A is the volume bounded by the surface Σ and

$$\frac{d\mathcal{W}}{dt} = \tau_{ij} \dot{e}_{ij}. \quad (9)$$

Note that the volume energy density function \mathcal{W} is not an elastic potential. It applies to an irreversible and dissipative process. The dot represents differentiation with time. The nine displacement gradients are e_{ij} given by

$$e_{ij} = \frac{\partial u_i}{\partial \xi_j}, \quad i, j = 1, 2, 3. \quad (10)$$

No limitations have been placed on the finiteness and/or magnitude of the deformation. When \mathcal{W} is interpreted as an isoenergy density function, it has the unique property that

$$\begin{aligned} \mathcal{W} &= \int \tau_{11} de_{11} = \int \tau_{12} de_{12} = \cdots \\ &= \int \tau_{23} de_{23} \rightarrow \int \tau de. \end{aligned} \quad (11)$$

This means that any one of the nine pairs $(\tau_{11}, e_{11}), (\tau_{12}, e_{12}), \dots, (\tau_{23}, e_{23})$ or (τ, e) can be

used to yield the same \mathcal{V} . Hence, the uniaxial isostress τ versus the isostrain e plot provides a general description of the energy state, even though the other stress components τ_{ij} are also acting on the element.

2.5. Synchronization of temperature and deformation

The nonequilibrium temperature Θ can be determined directly from \mathcal{V} , e and \mathcal{D} without introducing the concept of heat. Here, \mathcal{D} stands for the dissipation energy density

$$d\mathcal{D} = d\mathcal{V} - d\mathcal{A}, \quad \mathcal{D} \geq 0, \quad (12)$$

with \mathcal{A} being the available energy density. The dissipated and available energy are mutually exclusive and hence there is no loss in generality in the linear dependence state in Eq. (12). Derived in [4] is the relation

$$\frac{\Delta\Theta}{\Theta} = -\lambda \mathcal{V} \frac{\Delta e}{\Delta\mathcal{D}/\Delta e}, \quad (13)$$

where Θ represents the nonequilibrium temperature in contrast to T in classical thermodynamics that applies only to equilibrium states. The parameter λ relates the slope of the isostress τ isostrain e curve to the rate change of volume to surface dV/dA or \mathcal{V} , i.e.,

$$\tau = \int \lambda \mathcal{V} de. \quad (14)$$

2.6. Nonhomogenous response

Since both λ and \mathcal{V} can be computed from a knowledge of the deformation of each isoenergy element, only the values of τ and e or \mathcal{V} and e for the initial or reference state need to be known. Once the loading steps are specified, adjustment on (τ, e) can be made for each of the subsequent steps. In other words, the reference state from 0 to 1 in Fig. 1 or (\mathcal{V}^0, e^0) is assigned while the subsequent steps (\mathcal{V}^1, e^1) , (\mathcal{V}^2, e^2) , etc., are determined, the loci of which gives the response of a typical element. It is a self-adaptive procedure that accounts for the inhomogeneous response of the system.

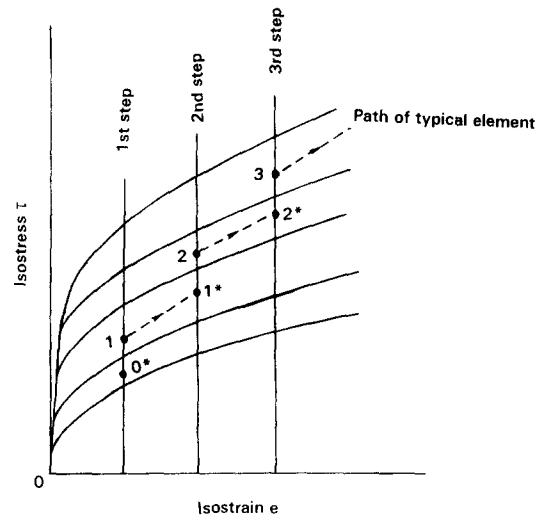


Fig. 1. Path of typical element in isostress and isostrain domain.

The foregoing procedure has been used to generate high strain rates uniaxial data beyond the range of present-day test machines. Data on complete stress and strain histories can be monitored only for strain rates no higher than 10 s^{-1} . Local strain rates for the impact problem at hand reach as high as 10^4 s^{-1} . Experimental checks can only be made at discrete points of the stress and strain curve.

3. Method of approach

Shown in Fig. 2 is a three-layer composite laminate with one-half symmetry. It is 20 mm in total thickness consisting of three different materials. A ceramic known as corundum (Al_2O_3) being the top layer is 6 mm thick. The middle rubber layer is 10 mm thick while the third layer is made of 4340 steel 4 mm thick. The staking sequence is selected so that the rubber can absorb and diffuse the initial surge in impact energy while the ceramic being hard momentarily slows down and breaks up an impacting tungsten rod with an initial mass m_0 of 0.128 kg and velocity v_0 of 1100 m/s.

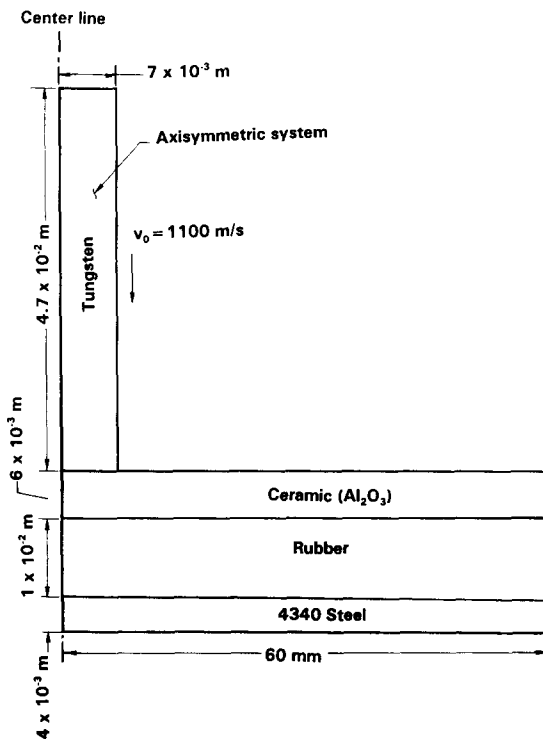


Fig. 2. Composite laminate subjected to normal impact.

3.1. Material data bank

As mentioned earlier, only the initial mechanical and fracture properties of the composite laminate need to be known. They are shown in Table 1. Once the system is disturbed by impact, the response of each material element will be derived individually in accordance with the displacement gradients and rate change of volume with surface. The data in Table 1 are referred to as the base properties.

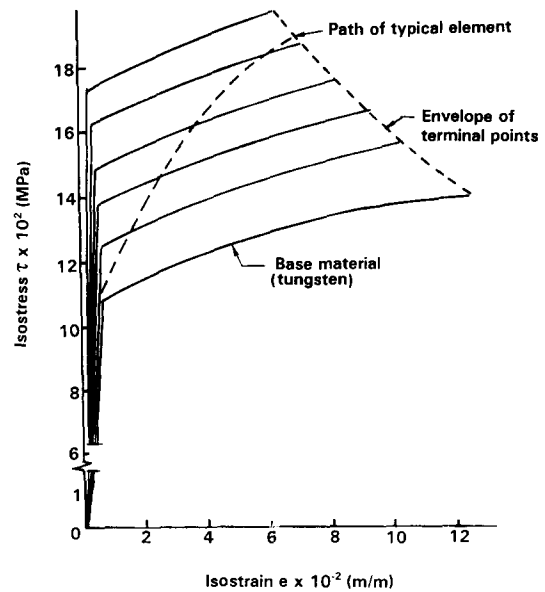


Fig. 3. Material data bank for tungsten.

Starting with the base material property of the tungsten rod, a material data bank may be constructed such that all points in the (τ, e) plane can be located in terms of \mathcal{V} . Some typical curves are displayed in Fig. 3. A great deal of accuracy can be achieved in determining a given state (\mathcal{V}, e) for each time increment by application of the floating data bank scheme. The terminal points of all the curves are governed by the yield strength σ_{ys} and fracture toughness \mathcal{W}_c relation shown in Fig. 4 for the tungsten. The path of a typical element in the isoenergy plane is shown in Fig. 3. It need not follow any one of the curves in the data bank which serves as a visual aid and to identify (τ, e) with (\mathcal{V}, e) .

Table 1
Mechanical and fracture base properties for the three-layer composite laminate

Material type	Young's modulus $E \times 10^{11}$ (Pa)	Mass density ρ (kg/m ³)	Yield strength $\sigma_{ys} \times 10^8$ (Pa)	Ultimate strength $\sigma_u \times 10^8$ (Pa)	Volume energy density $\mathcal{W}_c \times 10^5$ (Pa)
Tungsten	3.450	17 600	0.1062	0.1347	1.503×10^{-2}
Ceramic	4.650	19 350	0.3535	0.3535	1.344×10^{-2}
Rubber	4.0×10^{-7}	1100	7.500×10^{-6}	1.500×10^{-3}	2.176×10^{-1}
4340 steel	2.068	7850	9.70	11.00	115.60

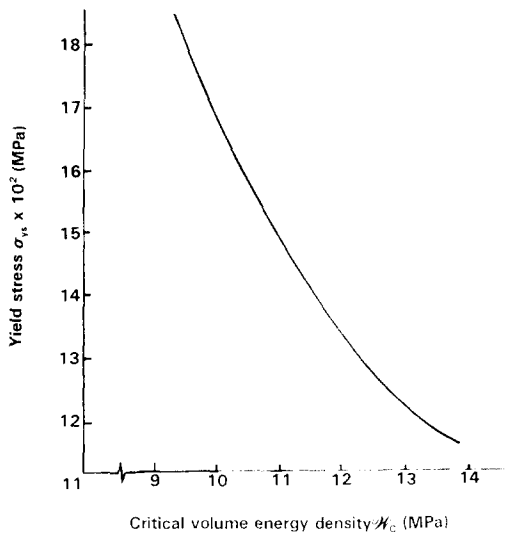


Fig. 4. Relation between yield strength and fracture toughness for tungsten.

The material bank for the ceramic layer is shown in Fig. 5. It consists of a group of straight lines because it is very hard in comparison with the other materials. This does not imply that all elements in the ceramic layer follow a linear stress and strain response. Linearity may not be preserved, as the actual behavior of a given element can cut across the family of straight lines in a nonlinear fashion as illustrated in Fig. 5. Again, the terminal points of the stress and strain curves in Fig. 5 are determined from the \mathcal{H}_c versus σ_{ys} .

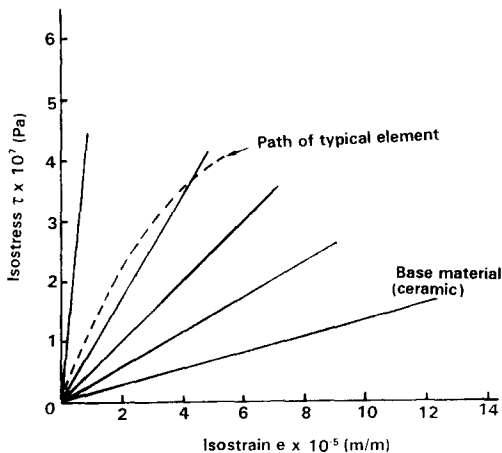


Fig. 5. Material data bank for the ceramic layer.

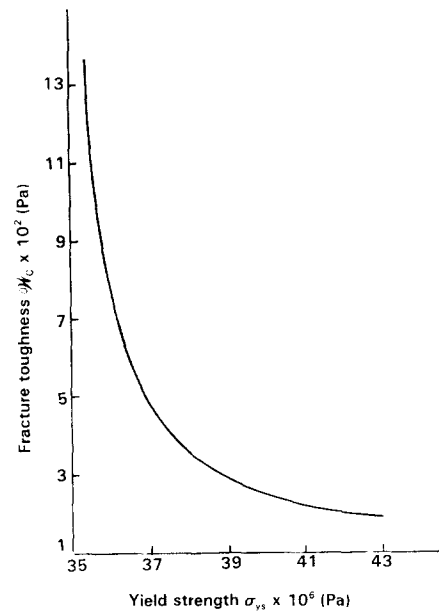


Fig. 6. Relationship between fracture toughness and yield strength for ceramic in material data bank.

relation in Fig. 6 for the ceramic. The response of the rubber to load is very different from that of the tungsten and ceramic materials discussed previously. Fig. 7 shows that \mathcal{V} or $d\tau/de$ can increase very rapidly. This feature is desirable from the energy absorption rate viewpoint, which will become evident when numerical results are made

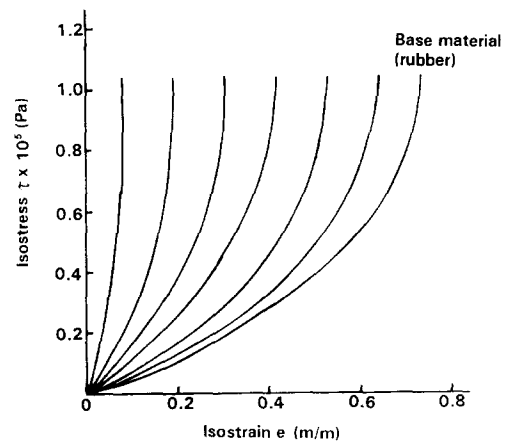


Fig. 7. Material data bank for rubber layer.

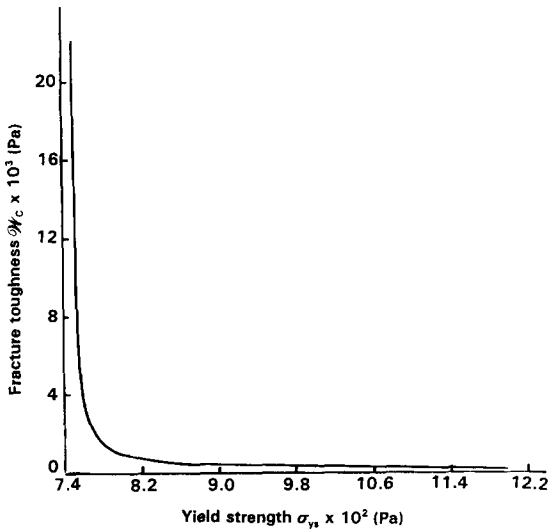


Fig. 8. Relationship between fracture toughness and yield strength for rubber in data bank.

available subsequently. A plot of \mathcal{H}_c against σ_{ys} for the rubber is given in Fig. 8.

The back-up layer is made of 4340 steel that contains the rubber and absorbs the excess energy transmitted through the first two layers. Fig. 9 and 10 provide the necessary data bank for the expediency of the numerical calculations.

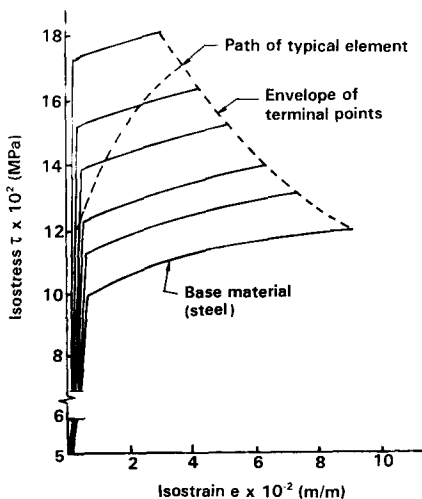


Fig. 9. Material data bank for 4340 steel.

3.2. Axisymmetric deformation

The tungsten rod is 47 mm in length and has a diameter of 14 mm. Axisymmetry is assumed to prevail at normal impact such that the configuration in Fig. 2 should be viewed as a body of revolution. Because of axisymmetry, only one angle β is required to locate the position of the isoenergy density element in the (ξ, η, ζ) plane as distinguished from the physical plane (x, y, z) or (r, θ, z) . According to [4], the corresponding displacements are

$$u_\xi = u_\xi(\xi, \zeta), \quad u_\eta = u_\eta(\eta, \zeta), \quad u_\zeta = u_\zeta(\xi, \zeta), \quad (15)$$

while the five nonvanishing deformation gradients are given by

$$e_\xi = \frac{\partial u_\xi}{\partial \xi}, \quad e_\eta = \frac{\partial u_\eta}{\partial \eta}, \quad e_\zeta = \frac{\partial u_\zeta}{\partial \zeta}, \quad f_\zeta = \frac{\partial u_\xi}{\partial \zeta}, \quad g_\xi = \frac{\partial u_\zeta}{\partial \xi}. \quad (16)$$

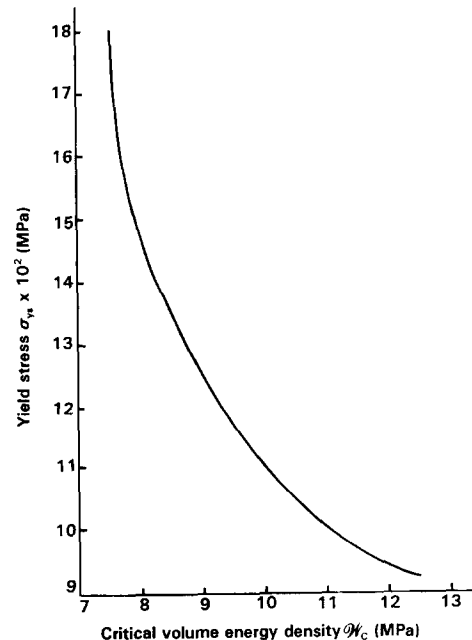


Fig. 10. Relation between yield strength and fracture toughness for 4340 steel.

The expressions for $(dV/dA)_i$ or \mathcal{V}_i take the form

$$\begin{aligned}\mathcal{V}_\xi = & \left\{ 2e_\eta + 2(e_\xi + e_\zeta)(1 + e_\eta) \cos \beta \right. \\ & + 2e_\xi e_\zeta \cos^2 \beta - (g_\xi^2 + f_\zeta^2) \sin^2 \beta - 2f_\xi g_\xi \} \\ & \times \left\{ [2e_\eta(1 + e_\zeta \cos \beta) + 2e_\zeta \cos \beta \right. \\ & \left. - f_\zeta^2 \sin^2 \beta] \cos \beta \right\}^{-1}, \\ \mathcal{V}_\eta = & \left\{ 2e_\eta + 2(e_\xi + e_\zeta)(1 + e_\eta) \cos \beta \right. \\ & + 2e_\xi e_\zeta \cos^2 \beta - (g_\xi^2 + f_\zeta^2) \sin^2 \beta - 2f_\xi g_\xi \} \\ & \times \left\{ 2[e_\xi + e_\zeta(1 + e_\xi \cos \beta)] \cos \beta \right. \\ & \left. - (g_\xi^2 + f_\zeta^2) \sin^2 \beta - 2f_\xi g_\xi \right\}^{-1}, \quad (17)\end{aligned}$$

$$\begin{aligned}\mathcal{V}_\zeta = & \left\{ 2e_\eta + 2(e_\xi + e_\zeta)(1 + e_\eta) \cos \beta \right. \\ & + 2e_\xi e_\zeta \cos^2 \beta - (g_\xi^2 + f_\zeta^2) \sin^2 \beta - 2f_\xi g_\xi \} \\ & \times \left\{ [2e_\eta(1 + e_\xi \cos \beta) + 2e_\xi \cos \beta \right. \\ & \left. - g_\xi^2 \sin^2 \beta] \cos \beta \right\}^{-1}.\end{aligned}$$

Even though the numerators and denominators of Eq. (17) contain only second-degree terms in e_ξ , e_η , etc., displacement gradient terms of order higher than second are included in the expansions for \mathcal{V}_i ($i = \xi, \eta, \zeta$). Because of axisymmetry, the condition

$$\mathcal{V}_\eta = \kappa = \text{const.} \quad (18)$$

may be assumed which, when applied to the second of Eqs. (17), renders

$$\begin{aligned}e_\eta = & \left\{ (\kappa - 1) [2(e_\xi + e_\zeta) \cos \beta \right. \\ & + 2e_\xi e_\zeta \cos^2 \beta - 2f_\xi g_\xi - (f_\zeta^2 + g_\xi^2) \sin^2 \beta] \} \\ & \times [2[1 + (e_\xi + e_\zeta) \cos \beta]]^{-1}. \quad (19)\end{aligned}$$

Hence, e_ξ and e_ζ are independent since e_η can be eliminated in view of Eq. (19). The condition of isoenergy in Eq. (4) may be further invoked to give

$$2(1 + e_\eta)(e_\xi - e_\zeta) \cos \beta - (g_\xi^2 - f_\zeta^2) \sin^2 \beta = 0. \quad (20)$$

Eq. (20) solves for β or the position of the isoenergy density element, since e_ξ , e_ζ , f_ζ and g_ξ are known functions of β , i.e.,

$$\begin{aligned}e_\xi &= e_r \cos^2 \beta + e_z \sin^2 \beta + (f_z + g_r) \sin \beta \cos \beta, \\ e_\zeta &= e_r \sin^2 \beta + e_z \cos^2 \beta - (f_z + g_r) \sin \beta \cos \beta, \\ f_\xi &= (e_z - e_r) \sin \beta \cos \beta + f_z \cos^2 \beta - g_r \sin^2 \beta, \quad (21)\end{aligned}$$

$$g_\xi = (e_z - e_r) \sin \beta \cos \beta - f_z \sin^2 \beta + g_r \cos^2 \beta.$$

The quantities e_r , e_z , f_z and g_r are computed numerically by a finite element procedure [9].

3.3. Computational procedure

The IDA program [9] is a finite element formulation of the isoenergy density theory. It solves for the displacements u_i that are up-dated for each increment of loading. The following steps are to be executed:

- Without loss in generality, start with an initial value of $\mathcal{V}^0 = 1$ mm and $d\tau/de$ from the base properties of the material. This also determines λ .
- The displacements u_i are found to yield e_r , e_z , f_z and g_r in Eqs. (21).
- Since e_ξ , e_ζ , f_ζ and g_ξ can now be related to e_r , e_z , f_z and g_r , the angle β in Eq. (20) can be determined.
- This gives dV/dA or \mathcal{V} together with e to establish a new (τ, e) state by using the initial λ .
- A segment of the path from 0^* to 1 as indicated in Fig. 1 is established.
- The foregoing process can thus be repeated to yield the subsequent segments.

The displacement gradients e_r , e_z , f_z and g_r referred to the physical coordinates (r, z) can be obtained from those referred to (ξ, ζ) using the relations:

$$\begin{aligned}e_r &= e_\xi \cos^2 \beta + e_\zeta \sin^2 \beta - (f_\zeta + g_\xi) \sin^2 \beta \cos \beta, \\ e_z &= e_\xi \sin^2 \beta + e_\zeta \cos^2 \beta + (f_\zeta + g_\xi) \sin \beta \cos \beta, \\ f_z &= -(e_\zeta - e_\xi) \sin \beta \cos \beta + f_\zeta \cos^2 \beta - g_\xi \sin^2 \beta, \quad (22) \\ g_r &= -(e_\zeta - e_\xi) \sin \beta \cos \beta - f_\zeta \sin^2 \beta + g_\xi \cos^2 \beta.\end{aligned}$$

The displacement gradients e_r and e_z should not be taken as the strain components in the classical continuum mechanics theory.

3.4. Damage thresholds

From a knowledge of the data bank established earlier, critical values of \mathcal{S} and \mathcal{W} or \mathcal{S}_c and \mathcal{W}_c can be computed for each element; they would change with time. Material damage states can be completely characterized by the trade-off between \mathcal{V} and \mathcal{W} .

Dominant surface energy density. When the surface energy density exceeds critical, i.e., $\mathcal{S} > \mathcal{S}_c$, the following two conditions prevail:

- $\mathcal{W} \approx \mathcal{W}_c$ — This corresponds to failure by frac-

ture over a region, the inside of which is also fragmented. Sliding nodes would be introduced between the fragments.

- $\mathcal{W} < \mathcal{W}_c$ — Gaps are created by fracture between material elements and accounted for by updating the grid pattern.

Dominant volume energy density. In situations where $\mathcal{W} > \mathcal{W}_c$ the surface energy density should be compared with its critical value \mathcal{S}_c :

- $\mathcal{S} \approx \mathcal{S}_c$ — Failure by massive fragmentation would be modelled. Material elements are dislodged and mass redistribution to neighboring nodes are made.
- $\mathcal{S} < \mathcal{S}_c$ — Fragmentation is not as severe, but mass redistribution would be needed to account for local damage.

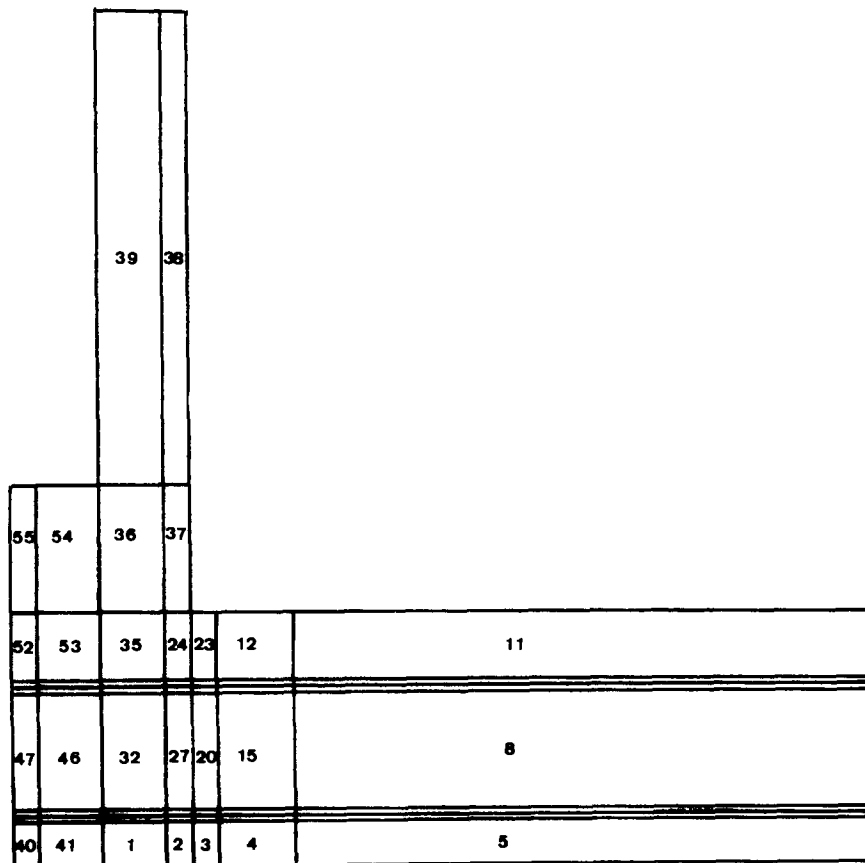


Fig. 11. Finite element grid pattern and element numbers for composite laminate and tungsten rod.

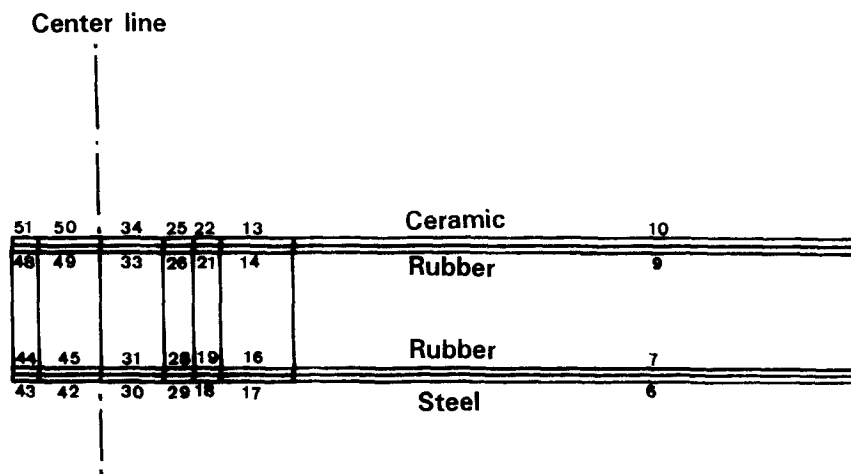


Fig. 12. Element numbers for ceramic/rubber and rubber/steel interface.

The initial time interval is selected to be sufficiently small such that none of the foregoing damage thresholds are exceeded.

4. Discussion of results: initial impact

The selection of the initial time interval involves several trial runs in order to gain a knowledge of response sensitivity for the disturbance in the composite laminate system. Unlike the single layer armor system [6], the changes in damage pattern are more tolerant to time variations. This is mainly due to the damping effect provided by the rubber layer. Only the results for $t = 0.150 \mu\text{s}$ will be discussed in Part I of the work. Presented

are the surface and volume energy density contours. Remeshing of the finite element grid pattern becomes necessary as the damage progresses and alters the connectivity of the elements. The latter will be considered in Part II [10].

4.1. Contact at impact

The twelve node isoparametric finite elements embedded with Gaussian points are employed to discretize the composite laminate system, as illustrated in Fig. 11. The center of axisymmetry coincides with the sides of elements 39, 36, 33, 32 and 1 such that the adjacent elements 54, 53, etc., are mapped across the center line to retain symmetry in the solution. Special attention is given to the

Table 2
Isostress, isostrain and isoenergy density at $t = 0.15 \mu\text{s}$

Material type	Element number	Isostress τ (MPa)	Isostrain $\epsilon \times 10^{-5}$ (m/m)	Surface energy density \mathcal{S} (N/m)	Volume energy density \mathcal{V} (Pa)
Ceramic	23	-0.00934	-0.00100	0.00513	0.00116
	24	0.00214	0.00024	0.00268	0.00060
	35	0.00695	0.00075	0.00084	0.00018
Rubber	20	-0.01372	-0.2368	0.53433	0.1943
	27	-0.01473	-0.2532	0.61874	0.2241
	32	-0.01091	-0.1923	0.29832	0.1086
Steel	3	-0.2399	-0.05805	0.03936	0.01984
	2	-0.2196	-0.05301	0.04014	0.02004
	1	-0.2256	-0.05459	0.03751	0.01869

interface elements in Fig. 12 which are labelled 51/48, 50/49, 34/33, 25/26, 22/21, 13/14 and 10/9 for the ceramic/rubber interface and 44/43, 45/42, 31/30, 28/29, 19/18, 16/17 and 7/6 for the rubber/steel interface. The surfaces between the dissimilar materials can move relative to one another.

Contact at impact is assumed to take place at $0.15 \mu\text{s}$. Results obtained from the IDA program show that the disturbance would first reach the elements under the impactor. They correspond to elements 1, 2, 3 and 4 for the steel; 15, 20, 27 and 32 for the rubber; and 17, 23, 24 and 35 for the ceramic. Their relative positions are shown in Fig. 11. Summarized in Table 2 are the isostress τ , isostrain e , surface isoenergy density \mathcal{S} and

volume isoenergy density \mathcal{W} . Even though their amplitudes are small, it is worthwhile to observe two important features of the solution at initial impact. While the rubber and steel are still in compression, reflective tensile waves have already reached elements 24 and 35 in the ceramic. These elements are directly under the impacting tungsten rod whereas element 23, being slightly away to the side of contact, is not affected by wave reflection. The larger tensile stress is in element 35, which is closest to the interior or farthest away from the edge of the impactor. Of interest is that the surface and volume energy density in the rubber are two orders and one order of magnitude larger than those in the ceramic and steel, respectively. This is a desirable feature of the

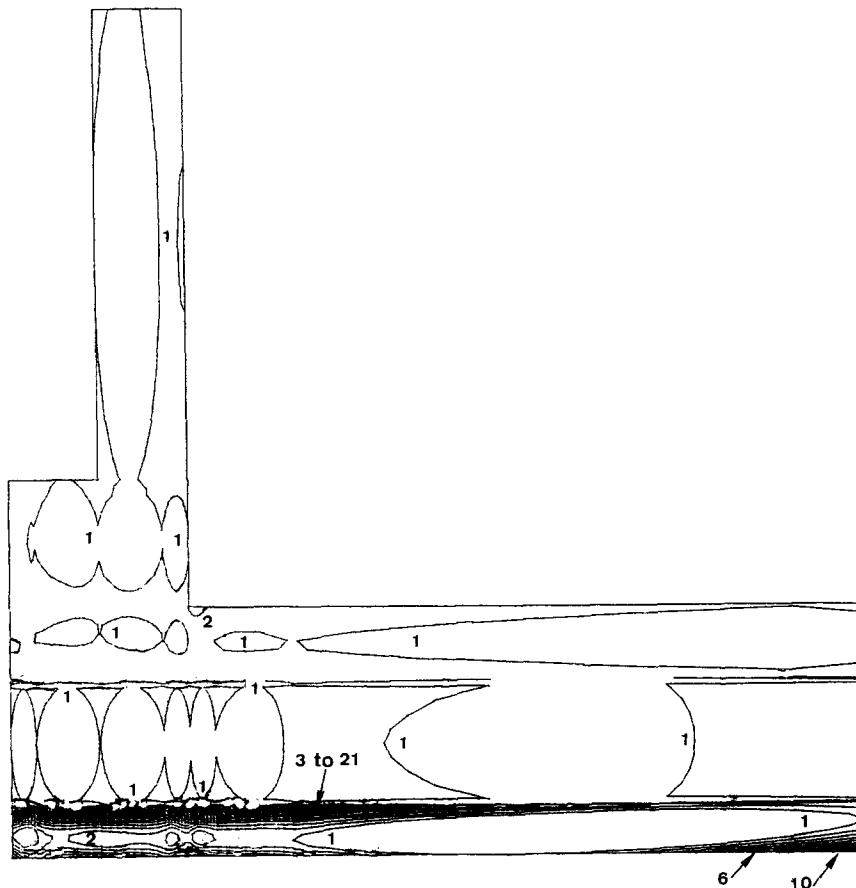


Fig. 13. Surface energy density in laminate.

Table 3
Surface isoenergy density values for contours in Fig. 13

Contour No.	\mathcal{S} (N/m)	Contour No.	\mathcal{S} (N/m)
1	0.56×10^{-9}	11	0.75×10^{-1}
2	0.75×10^{-2}	12	0.82
3	0.15×10^{-1}	13	0.90
4	0.22	14	0.97
5	0.30	15	0.10×10^0
6	0.37	16	0.11
7	0.45	17	0.12
8	0.52	18	0.13
9	0.60	19	0.13
10	0.67	20	0.14
		21	0.15

Table 4
Volume isoenergy density values for contours in Fig. 14

Contour No.	\mathcal{V} (Pa)	Contour No.	\mathcal{V} (Pa)
1	0.18×10^{-7}	11	0.87×10
2	0.87×10^0	12	0.96
3	0.17×10	13	0.10×10^2
4	0.26	14	0.11
5	0.35	15	0.12
6	0.44	16	0.13
7	0.52	17	0.14
8	0.61	18	0.15
9	0.70	19	0.16
10	0.79	20	0.17
		21	0.17

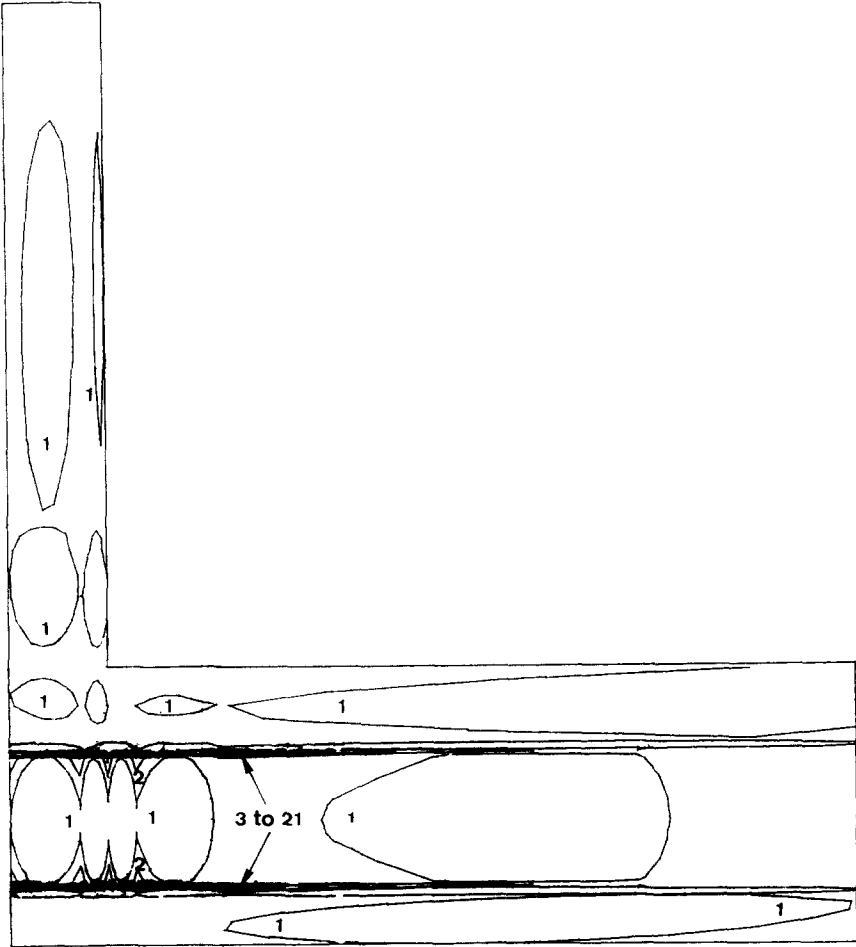


Fig. 14. Volume energy density in laminate.

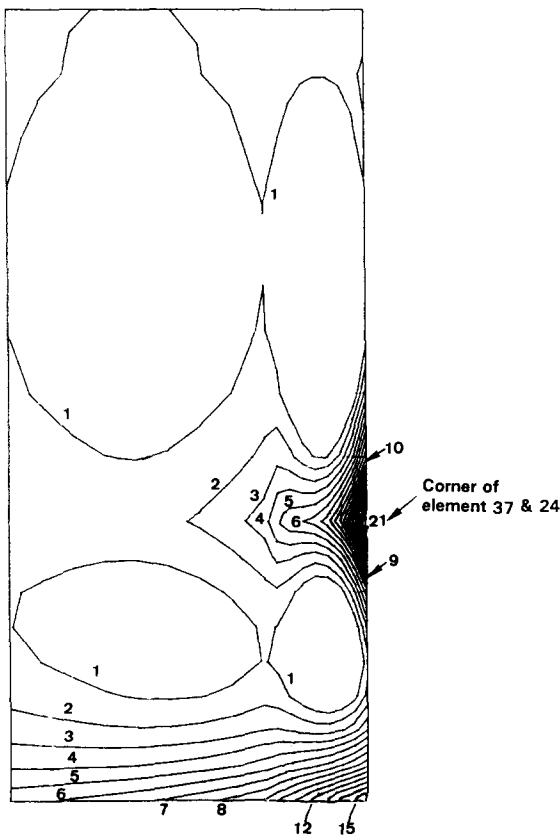


Fig. 15. Surface energy density near tungsten–ceramic interface.

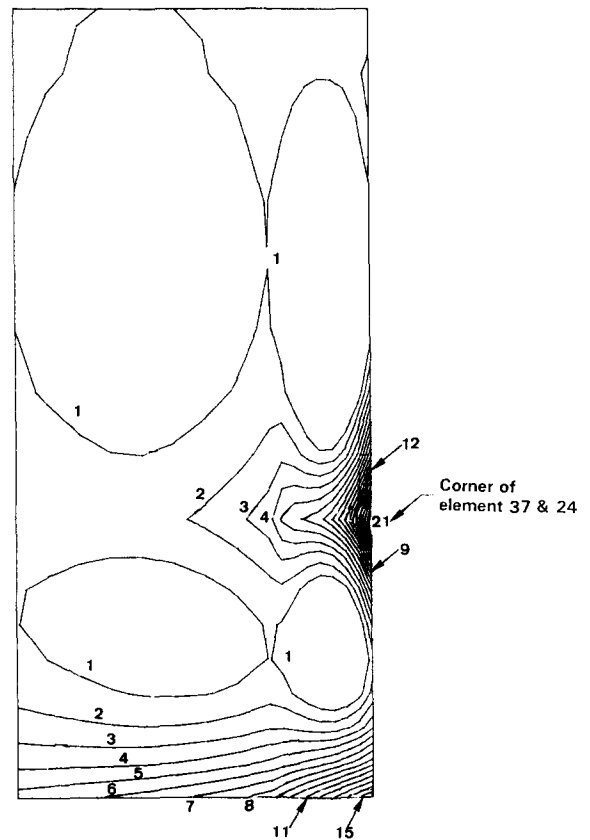


Fig. 16. Volume energy density near tungsten–ceramic interface.

laminate composite for otherwise the energy in the top and bottom layer would have been higher had the plate been made of a single material.

4.2. Isoenergy density contours

Plotted in Figs. 13 and 14 are, respectively, the \mathcal{S} and \mathcal{W} contours in the laminate composite $0.15 \mu\text{s}$ after impact. Note that energy has already been transmitted to all parts of the laminate, although the values of \mathcal{S} and \mathcal{W} are relatively low as shown in Tables 3 and 4.

Surface and volume energy concentrations at the reentrant corner where the tungsten rod comes into contact with the ceramic layer are illustrated in Figs. 15 and 16. The \mathcal{S} and \mathcal{W} contours are very closely packed at the corner. Table 5 shows a difference of five orders of magni-

tude for \mathcal{S} at the corner in comparison with the surface energy density values a distance away.

A similar situation prevails for the volume

Table 5
Surface isoenergy density values for contours in Fig. 15

Contour No.	\mathcal{S} (N/m)	Contour No.	\mathcal{S} (N/m)
1	0.19×10^{-6}	12	0.36
2	0.32×10^{-3}	13	0.39
3	0.65	14	0.42
4	0.97	15	0.45
5	0.13×10^{-2}	16	0.49
6	0.16	17	0.52
7	0.19	18	0.55
8	0.23	19	0.58
9	0.26	20	0.62
10	0.29	21	0.65
11	0.32		

energy density. This is shown by the contours in Fig. 16 where \mathcal{W} at the corner is elevated nearly five orders of magnitude. Refer to the numerical values in Table 6.

Localization of energy density at the ceramic/rubber interface is also clearly evidenced from the \mathcal{S} and \mathcal{W} contours in Figs. 17 and 18. High values of \mathcal{S} and \mathcal{W} are detected at the lower side of the ceramic layer where it comes into contact with the rubber. This effect is particularly pronounced at the corner of elements 22 and 25. Concentration of \mathcal{S} at the top of the ceramic layer where elements 23 and 24 meet is also noticeable in Fig. 17, but not for \mathcal{W} in Fig.

Table 6

Volume isoenergy density values for contours in Fig. 16

Contour No.	\mathcal{W} (Pa)	Contour No.	\mathcal{W} (Pa)
1	0.56×10^{-7}	11	0.76×10^{-3}
2	0.76×10^{-4}	12	0.84
3	0.15×10^{-3}	13	0.91
4	0.23	14	0.99
5	0.30	15	0.11×10^{-2}
6	0.38	16	0.11
7	0.46	17	0.12
8	0.53	18	0.13
9	0.61	19	0.14
10	0.69	20	0.14
		21	0.15

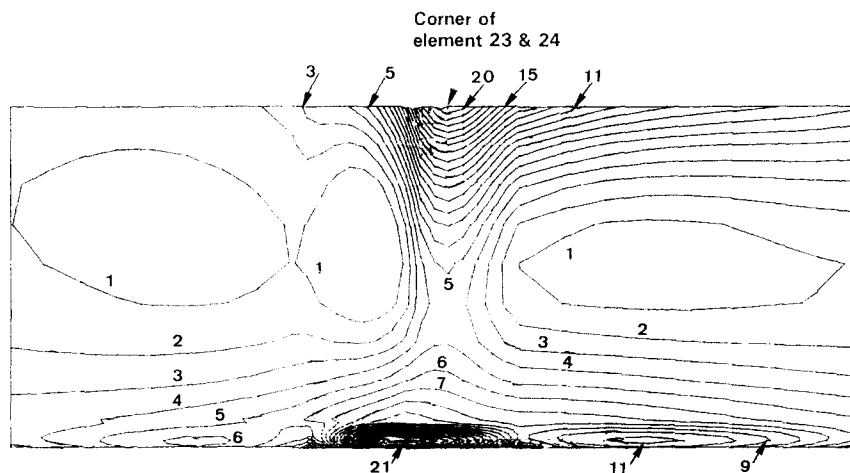


Fig. 17. Surface energy density in ceramic layer.

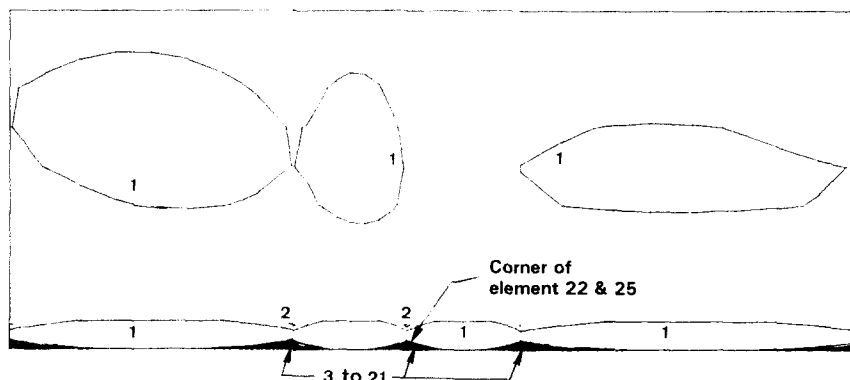


Fig. 18. Volume energy density in ceramic layer.

Table 7
Surface isoenergy density values for contours in Fig. 17

Contour No.	\mathcal{S} (N/m)	Contour No.	\mathcal{S} (N/m)
1	0.25×10^{-5}	11	0.57×10^{-2}
2	0.57×10^{-3}	12	0.63
3	0.11×10^{-2}	13	0.69
4	0.17	14	0.74
5	0.23	15	0.80
6	0.29	16	0.86
7	0.34	17	0.91
8	0.40	18	0.97
9	0.46	19	0.10×10^{-1}
10	0.51	20	0.11
		21	0.11

Table 8
Surface isoenergy density values for contours in Fig. 18

Contour No.	\mathcal{W} (Pa)	Contour No.	\mathcal{W} (Pa)
1	0.53×10^{-6}	11	0.71×10
2	0.71×10^0	12	0.78
3	0.14×10	13	0.85
4	0.21	14	0.92
5	0.28	15	0.99
6	0.35	16	0.11×10^2
7	0.43	17	0.11
8	0.50	18	0.12
9	0.57	19	0.13
10	0.64	20	0.13
		21	0.14

18. The corresponding contour values of \mathcal{S} and \mathcal{W} can be found in Tables 7 and 8, respectively.

In contrast to the energy density distributions for the ceramic layer in Figs. 17 and 18, Figs. 19 and 20 reveal that the volume energy tends to dominate in the rubber rather than the surface energy density.

Fig. 19 displays the \mathcal{S} contours which tend to congregate at the corner of elements 21 to 26 at the top and elements 19 and 28 at the bottom. Their locations with reference to the entire laminate are shown in Figs. 11 and 12. The highly packed contours of \mathcal{W} near the top and bottom layer in Fig. 20 are evidence of volume energy

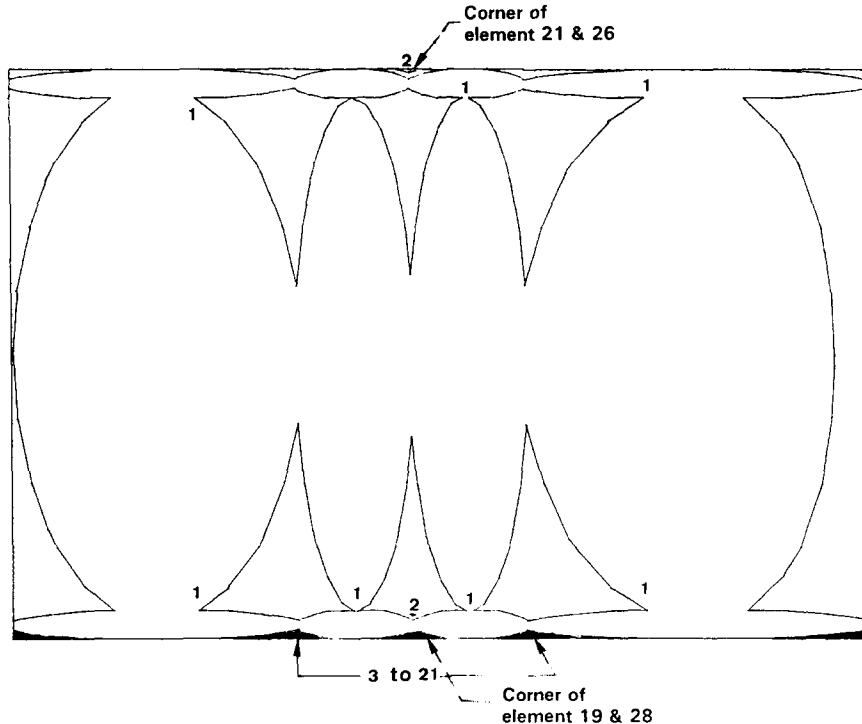


Fig. 19. Surface energy density in rubber layer.

Table 9
Surface isoenergy density values for contours in Fig. 19

Contour No.	\mathcal{S} (N/m)	Contour No.	\mathcal{S} (N/m)
1	0.74×10^{-8}	11	0.43×10^{-1}
2	0.43×10^{-2}	12	0.47
3	0.86	13	0.52
4	0.13×10^{-1}	14	0.56
5	0.17	15	0.60
6	0.22	16	0.65
7	0.26	17	0.69
8	0.30	18	0.73
9	0.34	19	0.77
10	0.39	20	0.82
		21	0.86

Table 10
Volume isoenergy density values for contours in Fig. 20

Contour No.	\mathcal{V} (Pa)	Contour No.	\mathcal{V} (Pa)
1	0.28×10^{-1}	11	0.88×10
2	0.90×10^0	12	0.97
3	0.18×10	13	0.11×10^2
4	0.27	14	0.11
5	0.35	15	0.12
6	0.44	16	0.13
7	0.53	17	0.14
8	0.62	18	0.15
9	0.70	19	0.16
10	0.79	20	0.17
		21	0.18

trapped at the top interface with ceramic and bottom with steel. Tables 9 and 10 gives the values of \mathcal{S} and \mathcal{V} .

The surface and volume energy density contours in the back-up 4340 steel layer are shown in Figs. 21 and 22. Concentration of energy density again prevails at the rubber/steel interface while the energy level elsewhere is not significant. Numerical values of the contours associated with \mathcal{S}

and \mathcal{V} can be found in Tables 11 and 12, respectively.

5. Conclusions

Analysis of failure behavior in composite laminates can be complex if detailed information is required on the nonhomogeneous nature of the

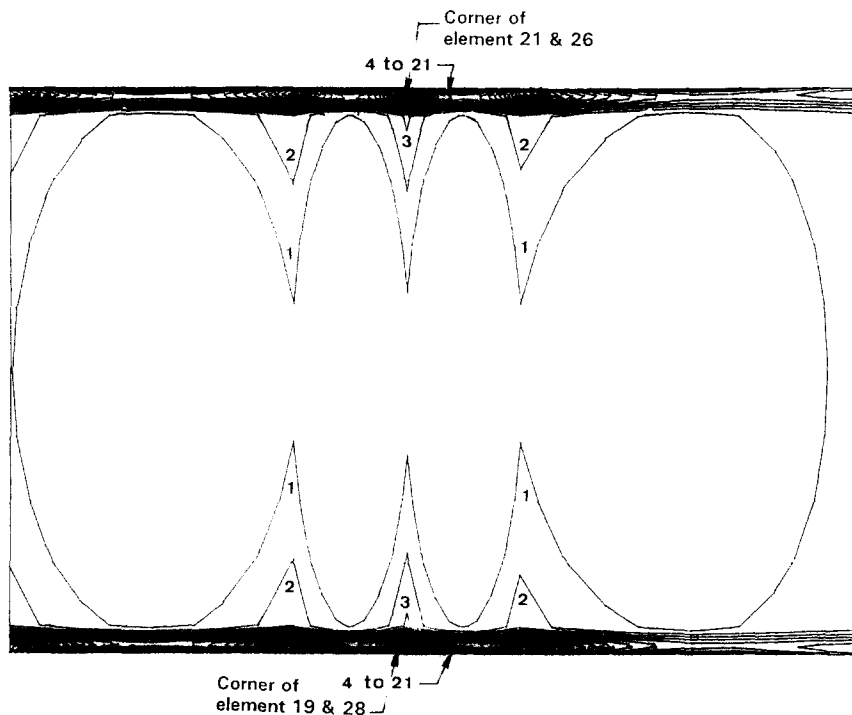


Fig. 20. Volume energy density in rubber layer.

Table 11
Surface isoenenergy density values for contours in Fig. 21

Contour No.	\mathcal{S} (N/m)	Contour No.	\mathcal{S} (N/m)
1	0.51×10^{-3}	11	0.71×10^{-1}
2	0.75×10^{-2}	12	0.78
3	0.15×10^{-1}	13	0.85
4	0.22	14	0.92
5	0.29	15	0.99
6	0.36	16	0.11×10^0
7	0.43	17	0.11
8	0.50	18	0.12
9	0.57	19	0.13
10	0.64	20	0.13
		21	0.14

Table 12
Surface isoenenergy density values for contours in Fig. 22

Contour No.	\mathcal{W} (Pa)	Contour No.	\mathcal{W} (Pa)
1	0.25×10^{-3}	11	0.71×10
2	0.71×10^0	12	0.78
3	0.14×10	13	0.85
4	0.21	14	0.92
5	0.28	15	0.99
6	0.35	16	0.11×10^2
7	0.43	17	0.11
8	0.50	18	0.12
9	0.57	19	0.13
10	0.64	20	0.13
		21	0.14

damage process that changes progressively with the load history. When the energy is transferred from one body to another over a localized region in a short period of time as in the case of impact,

additional allowance must be made to account for the wide range of strain and strain rates that the material would experience.

Part I of this study provided the methodology

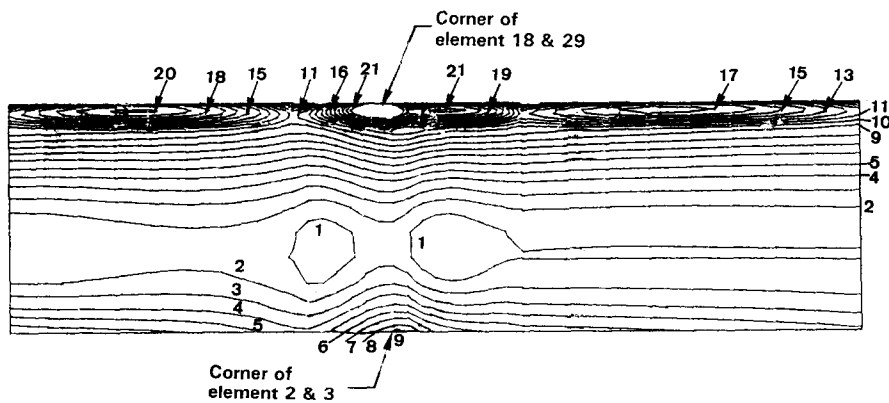


Fig. 21. Surface energy density in 4340 steel layer.

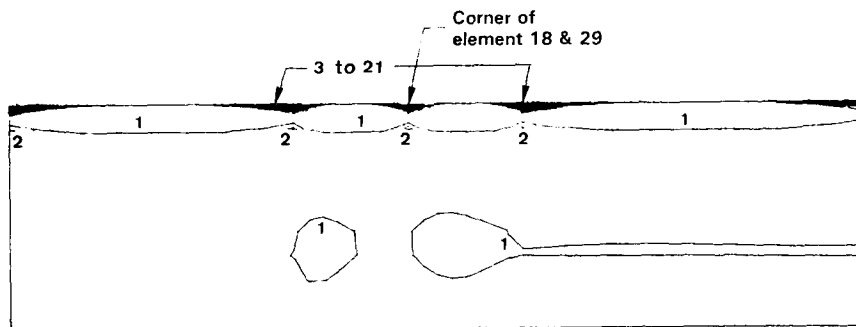


Fig. 22. Volume energy density in 4340 steel layer.

for deriving the dynamic stress and strain response in each element of a three-layered composite laminate impacted by a tungsten rod at high speed. The concept of isoenergy elements is employed such that the base material properties obtained from uniaxial tests would be applied to predict the behavior of elements under multi-axial stress and strain states. Time scales of the order of 10^{-1} μ s were found to coincide with the period of initial contact. The highly nonhomogeneous character of the dynamic disturbance was already evident. The surface and volume energy density near the impact site and interfaces were elevated four to five orders of magnitude. Changes in the sign of the stresses are indicative of the effect of wave reflection. Application of the isoenergy density theory has also been made to evaluate the shock response of unidirectional and laminate composites damaged by high power laser [11].

Damage evolution of the ceramic/rubber/steel laminate is presented in Part II [10]. As the local damage alters the morphology of the laminate structure, the finite element grid pattern needs to be remeshed for each time step. This process is continued until the tungsten rod is completely disintegrated at approximately 21.5 μ s after impact. Data on the local temperature and dissipation energy density will also be given in Part II to ascertain the thermal properties of the laminate.

Acknowledgements

The author wishes to acknowledge Dr. D.Y. Tzou for his effort on the computational aspect of this work when he was at Lehigh University.

References

- [1] G.C. Sih, *Mechanics of Projectile / Target Systems* (Newell Company: Allentown, PA, 1991).
- [2] G.C. Sih, Diagnostic Aspects of Armor Penetration and Protection, Lectures Chung-Cheng Institute of Technology, Taiwan, pp. 1–237 (1994).
- [3] Foreign Object Impact Damage to Composites, American Society of Testing Materials, STP 568, Philadelphia, PA (1975).
- [4] G.C. Sih, Thermomechanics of solids: nonequilibrium and irreversibility *J. Theor. Appl. Fract. Mech.* 9, 175–198 (1988).
- [5] G.C. Sih, Some problems in nonequilibrium thermomechanics, *Advances in Thermodynamics Vol. 6: Flow, Diffusion and Rate Processes*, eds. S. Sieniutycz and P. Slamon (Taylor and Francis: New York, 1992) 218–247.
- [6] G.C. Sih, Thermal/mechanical penetration damage of 4340 steel impacted by tungsten projectile, *Advances in Numerical Simulation Techniques for Penetration and Perforation of Solids*, Vol. 171 eds., E.P. Chen and V.R. Luk (ASME, Applied Mechanics Division, 1993) 133–145.
- [7] G.C. Sih, Initial damage states of hypervelocity impact for tungsten projectile on aluminum target, *J. Theor. Appl. Fract. Mech.* 13, 167–180 (1990).
- [8] P.W. Mast, G.E. Nash, J. Michopoulos, R.W. Thomas, R. Badalian and I. Wolock, Characterization of strain-induced damage in composites based on the dissipated energy density: Part I — Basic scheme and formation; Part II — Composite specimens and naval structures; and Part III — General material constitutive relation, *J. Theor. Appl. Fract. Mech.* 22 (2), 71–125 (1995).
- [9] G.C. Sih and D.Y. Tzou, Isoenergy density analysis (IDA), Institute of Fracture and Solid Mechanics Technical Report (1988).
- [10] G.C. Sih, Impact damage of laminated composite with energy dissipation: Part II — Damage evolution, *J. Theor. Appl. Fract. Mech.* 22 (3), 189–218 (1995).
- [11] G.C. Sih, Shock response of unidirectional and laminate composite damaged by high power laser, Technical Report: Naval Research Laboratory contract No. N00014-88-C-2089, March (1989).